Large-Eddy-Simulation of flow and heat transfer in a ribbed duct

O. Labbé
ONERA - The French Aerospace Lab
F-92322 Châtillon, France

Abstract

Large-eddy simulations investigate turbulent flow and heat transfer in a ribbed channel, with parameters reproducing the experiments of Casarsa et al. [4]. Two simulations are carried out. The first one consists in a full domain including five ribs representing the experimental test section and aims to verify the flow periodicity found experimentally. In this case, inflow and outflow boundary conditions are used in the streamwise direction. The second simulation, restricted to one pitch length with periodic conditions applied in the streamwise direction, aims to check if this simple configuration is able to reproduce the experiments. Mean and turbulent quantities together with the heat transfer of both simulations are compared to experimental data.

1. Introduction

In heat exchanger applications, ducts with rib turbulators are used to increase the convective heat transfer. Accurate prediction of ribbed duct flow and heat transfer is of importance to the gas turbine industry. Flows generated by ribs are dominated by separating and reattaching shear layers with vortex shedding and secondary flows in the cross-section. A wide database of experimental data for ribbed ducts in many geometric configurations and flow conditions is available in the literature (Han (1988) [8]; Liou et al. (1993) [10]; Çakan (2000) [3]; Casarsa et al. (2002) [4]; Chandra et al. (2003) [5]; Graham et al. (2004) [6]; Tanda (2004) [16]; Won and Ligrani (2004) [19]; Arun and Prabhu (2007) [1]; Gupta et al. (2008) [7]. Computational studies have also been used extensively in investigating flow and heat transfer effects in ribbed ducts. Prediction of these flows has been complicated by the presence of separating/reattaching shear layers, secondary flows. The flow is affected by the sidewalls and a three-dimensional representation is needed. The Reynolds-averaged Navier-Stokes (RANS) turbulence modelling does not have the accuracy required of a prediction tool across the wide range of physical phenomena encountered in internal cooling flows. By resolving only energy containing eddies, Large-Eddy Simulation (LES) reduces the computational complexity of direct numerical simulations (DNS) by several orders of magnitude. Among the studies, which consider 3D flow, one may list: Murata and Mochizuki (2001) [13], Watanabe and Takahashi (2002) [18], Tafti (2005) [15], Sewall et al. (2006) [14]; Viswanathan and Tafti (2006) [17], Liu and Wang (2011) [11]. The large-eddy simulations carried out by Lohász et al. (2005) [12] reproduce the experiments of Casarsa et al. (2002) [4] without taking into account the heat transfer. The papers mentioned above solve the Navier-Stokes equations for an incompressible flow and a temperature equation which acts like a passive scalar.

2. Square ribbed channel

The present contribution concerns the simulation of the flow in a square duct where successive ribs of square cross section are mounted on the lower wall perpendicularly to the stream direction. Casarsa et al. [4] have experimentally found that for such a configuration the flow starts to repeat itself in every pitch length after the fourth rib. Two simulations are carried out: the first one, referenced later by LES-F, consists in a full domain including five ribs, the length of which in the streamwise (X) direction attempts to represent the experimental test section. In this case, inflow and outflow boundary conditions are used in the streamwise (X) direction. The second simulation (LES-P) is confined around a single rib and uses periodic conditions in the streamwise (X) direction. The numerical results will be compared with those obtained experimentally between the fourth and fifth ribs.

The channel is characterized by a square cross section (Y, Z) 0.1x0.1 m2. The rib cross section (hxh) is 0.03x0.03 m^2, providing a blockage ratio of 30%. The pitch-to-height ratio (P/h) is equal to 10. The Reynolds number of the mean flow based on the hydraulic diameter D_h and the bulk velocity is equal to 4.104. The duct walls as well as the three faces of the ribs exposed to the main flow are heated by imposing a constant heat flux q_w = 650 W/m^2 prescribed in the experiments. Fig. 1 displays the computational domain with five obstacles (top) and the periodic domain (bottom).

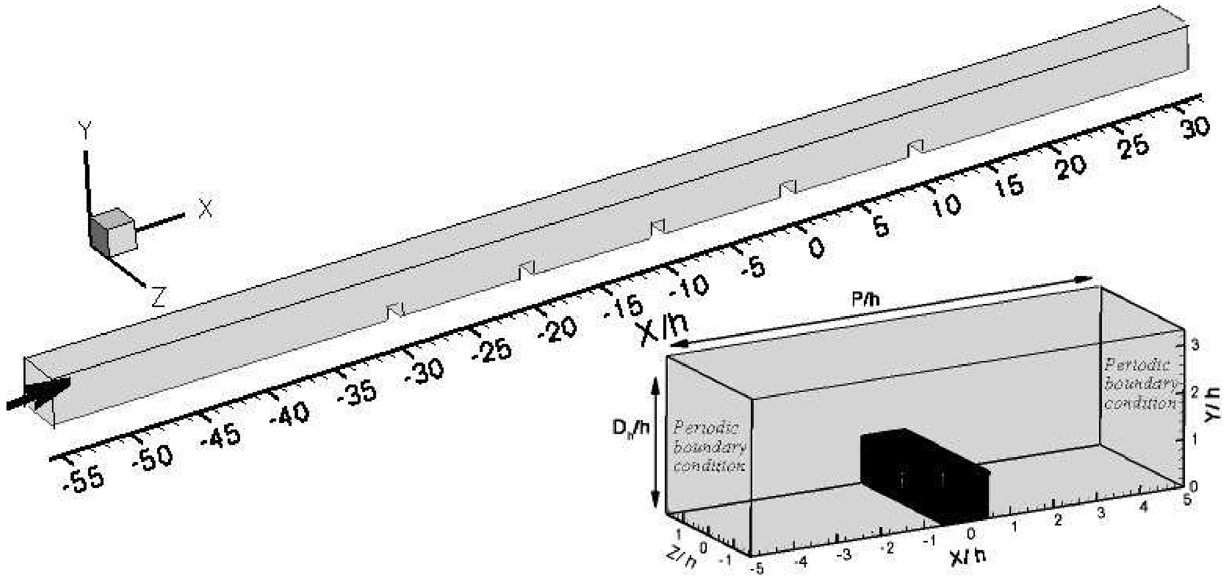

Figure 1: Full and periodic computational domains.

3. Governing equations and computational model

The time-accurate resolution method of complex flows, which present separating /reattaching shear layers and secondary flows is based on the large-eddy simulation. LES, by solving the energy containing eddies, reduces the complexity of Direct Numerical Simulation (DNS) by several orders of magnitude. Two approaches are commonly used to perform LES: explicit subgrid stress models are used to represent the effect of unresolved scales of motion on the large scales and the second method consists in using the Monotonic Integrated Large-Eddy Simulations (MILES) proposed by Boris et al. [2]. This latter is based on the assumption that the intrinsic dissipation of an upwind scheme is able to mimic the dissipative behaviour of the unresolved turbulent scales, and that when using such a scheme, the subgrid viscosity has to be set to zero. The MILES approach has been used in the present study. The governing equations for LES are the grid-filtered mass, momentum and total energy equations for compressible flow. In order to simplify the resulting set of equations, a mass-weighted change of variable (Favre) is defined as: $\overline{\rho f} = \bar{\rho}\tilde{f}$

$$\frac{\partial\bar{\rho}}{\partial t} + \frac{\partial}{\partial x_j}(\bar{\rho}\,\tilde{u}_j) = 0 \tag{1}$$

$$\frac{\partial}{\partial t}(\bar{\rho}\,\tilde{u}_i) + \frac{\partial}{\partial x_j}(\bar{\rho}\,\tilde{u}_i\tilde{u}_j) + \frac{\partial\bar{p}}{\partial x_i} - \frac{\partial\tilde{\sigma}_{ij}}{\partial x_j} = -\alpha\,\delta_{i1} \tag{2}$$

$$\frac{\partial\,\rho\hat{E}}{\partial t} + \frac{\partial}{\partial x_j}\left\{(\rho\hat{E} + \bar{p})\tilde{u}_j\right\} - \frac{\partial}{\partial x_j}(\tilde{\sigma}_{ij}\,\tilde{u}_i) + \frac{\partial\tilde{q}_j}{\partial x_j} = -\alpha\,\tilde{u}_1 - \bar{\rho}\tilde{u}_1\beta \tag{3}$$

where the total energy is written as follows: $\rho\hat{E} = \frac{\bar{p}}{\gamma-1} + \frac{1}{2}\bar{\rho}\,\tilde{u}_j\tilde{u}_j$. The stress tensor $\tilde{\sigma}_{ij}$ is defined as: $\tilde{\sigma}_{ij} = \mu(\tilde{T})(\frac{\partial\tilde{u}_i}{\partial x_j} + \frac{\partial\tilde{u}_j}{\partial x_i} - \frac{2}{3}\frac{\partial\tilde{u}_k}{\partial x_k}\delta_{ij})$. The heat flux vector is given by: $\tilde{q}_j = -\frac{\mu(\tilde{T})}{(\gamma-1)Re\,\mathrm{Pr}\,M^2}\frac{\partial\tilde{T}}{\partial x_j}$.

In case of inflow/outflow boundary conditions in the streamwise direction the coefficients α and β are equal to zero, but in case of periodicity conditions in the simulation the term α is the mean pressure gradient to balance the wall-shear stress on the walls, it is imposed in the streamwise direction to maintain a constant flow rate and δ_{i1} takes the value of one when i=1. A mean enthalpy gradient β is added in order to balance the global energy due to the heated walls, $\beta = q_w S_w / \dot{m}P$ where q_w is the heat flux at the walls, S_w the total surface of the heated walls, $\dot{m}$ the flow rate and P is the pitch distance. To close the set of equations, the following filtered equation of state is used: $\tilde{p}/\overline{\rho} = r\tilde{T}$ with r =287 J kg^{-1} K^{-1}. The viscosity dependence on temperature is modelled using the Sutherland's law.

4. Simulation characteristics

Mesh density is relatively high in the vicinity of the rib and the duct surfaces to resolve the boundary /shear layers, which is crucial to the accurate prediction of turbulence and heat transfer. For the periodic domain, the computational grid consists in about 5.2 million grid points, which are distributed as follows: 301 and 101 grid points respectively in the streamwise and spanwise directions. In the vertical direction 201 (121 above the rib) grid points are used. The full domain consists in 5 periodic computational domains, plus a zone at the entrance (301x201x101) and a zone at the outflow (301x201x101). All in all in the full domain there are 38 million grid points. The time step is set to 3.10^{-6} D$_h$/U$_0$ leading to a maximum local CFL number of 0.6.

The grid points are clustered in the vicinity of the walls and the size of the first cell is 0.0003D$_h$ near the walls. The quality of the resolution is judged by determining the cell size in wall units based a posteriori on the mean wall shear velocity. To evaluate the resolution at the near-wall region, the most important criterion is the distribution of non-dimensional y_1^+ and z_1^+ which represent the size of the first cell on the bottom and lateral walls from LES-P. Fig. 2 depicts the y_1^+ and z_1^+ distribution in the half lower (left) and lateral (right) walls. The highest value of y_1^+ is found on the rib top and near the lateral wall before the rib, while z_1^+ is very low <1, except at the leading edge of the lateral wall .The simulation resolves the walls by a DNS-like representation (y_1^+, z_1^+<1).

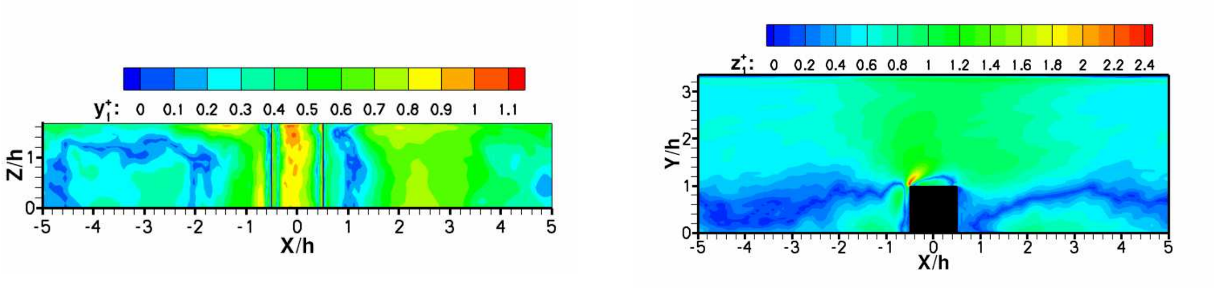

Figure 2: Distribution of y_1^+ (left) on the half lower wall and z_1^+ (right) on the lateral wall.

The governing equations for mass, momentum and energy are discretized with a conservative finite-volume formulation. The spatial discretization method is based on the cell-centred finite volume methodology. An upwind biased, with a third-order MUSCL interpolation scheme of AUSM+(P) family without any shock capturing feature is used for the convective scheme. An explicit time integration is carried out by means of a third-order compact Runge-Kutta scheme. Details of the method can be found in Larchevêque et al. [9]. In the first configuration at the inflow boundary, thermo-dynamic state is imposed, while at the outflow boundary the non-reflecting characteristics are applied. In the second configuration, periodic boundary conditions are imposed in the streamwise (X) direction. No-slip boundary conditions and wall temperature are applied at the top, bottom and lateral walls of the channel and at the top and lateral walls of the rib.

5. Results

All the results presented in this section are time-averaged quantities. The flow is strongly three-dimensional. The combined effect of the rib and the side walls induces secondary flows in the cross-section of the channel. As a matter of fact the blockage forces the flow in front of the rib to swirl toward the lateral walls in an upward motion over the rib which is noticeable in Fig. 3 (left) corresponding to LES-P. In this latter, the streamlines started from a line upstream from the rib, are spiralling in front of it, forming a surface trapped in the upstream corner. This forces the flow to swirl towards the walls above the rib and to finally escape downstream in the channel corner. The presence of the high spanwise velocity regions upstream of the rib is due to the blockage effect of the rib. The secondary cross-sectional flows have a large impact on the heat transfer augmentation on the side walls.

Considering the mean flow in the center plane Z/h=0, Fig. 3 (right) reveals four distinct zones associated with the rib. A wide recirculation bubble occurs downstream from the rib due to the sudden expansion of the flow, accompanied by a small counter rotating vortex V1 at the lower corner behind the rib. After the flow reattachment line (L$_R$), a new boundary layer develops and impinges on the next rib forming an upstream vortex V3. Another recirculation zone V2 is formed on the rib top as the sharp front edge of the rib deflects the flow. The mesh is sufficiently refined to reveal other small counter-vortices in the corners, which size are ΔX/h =0.02, and another vortex on the rib top, just behind

V2. The Table 1 compares the size of the different recirculation zones for both LES presented here as well as the Lohász et al. LES [12] with the experimental data [4].

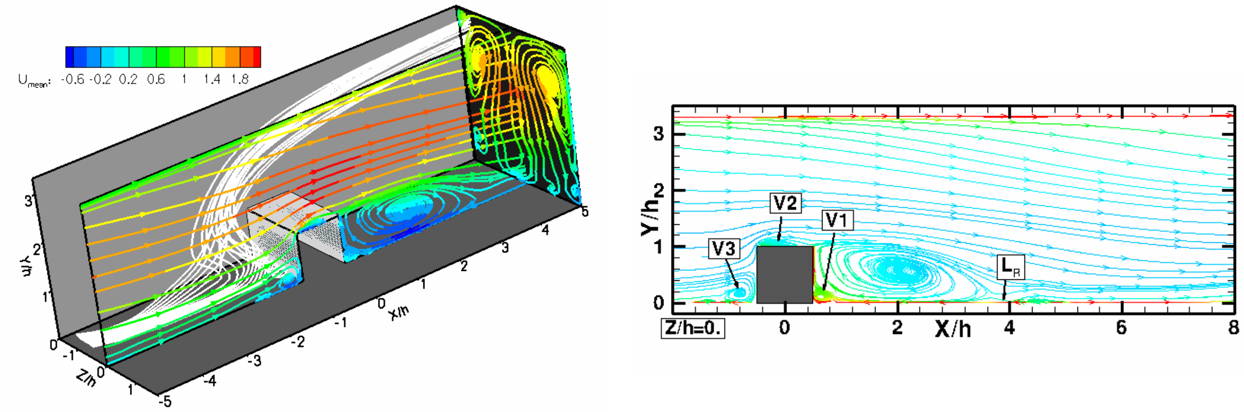

Figure 3: (Left) Global flow view, the streamlines are colored with mean streamwise velocity. (Right) Details of flow structures around the rib at the center plane.

Table 1: Comparison of the different recirculation zones.

	Casarsa et al. [4]	LES (Lohász et al.) [12]	LES-F	LES-P
Reattachment length	$4.26<X/h<4.34$	$\Delta X/h = 3.85$	$\Delta X/h = 4.23$	$\Delta X/h = 3.71$
V1	$0.25 < \Delta X/h < 0.28$	$\Delta X/h = 0.5$	$\Delta X/h = 0.37$	$\Delta X/h = 0.41$
V2	$0.6<\Delta X/h<0.9$	$\Delta X/h = 0.91$	$\Delta X/h = 0.84$	$\Delta X/h = 0.91$
V3	$1.04<\Delta X/h<1.5$	$\Delta X/h = 0.66$	$\Delta X/h = 0.7$	$\Delta X/h = 0.6$

Fig. 4 shows contours of mean streamwise velocity at the center plane Z/h=0, negative values are represented with dashed lines. The iso-contours of the LES-F (top) confirm a global periodicity of the flow. The LES-F (top) and LES-P results (right-bottom) are in good agreement with those obtained experimentally by Casarsa et al. (left-bottom). The rib reduces the cross section and consequently accelerates the flow and high velocity gradients are found in the upstream top corner rib. The sudden expansion downstream from it, leads to a reverse flow boundary, which grows in thickness in the upstream direction, along the length of the recirculation zone.

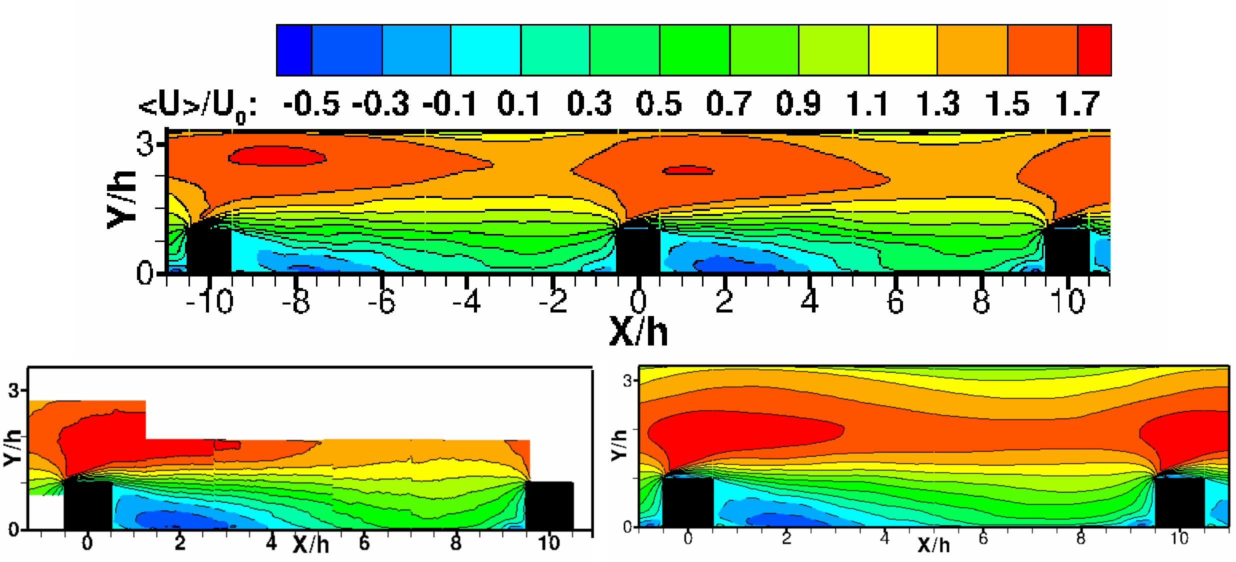

Figure 4: U_{mean} at the center plane, LES-F (top), LES-P (right-bottom), Casarsa et al. [4] (left-bottom).

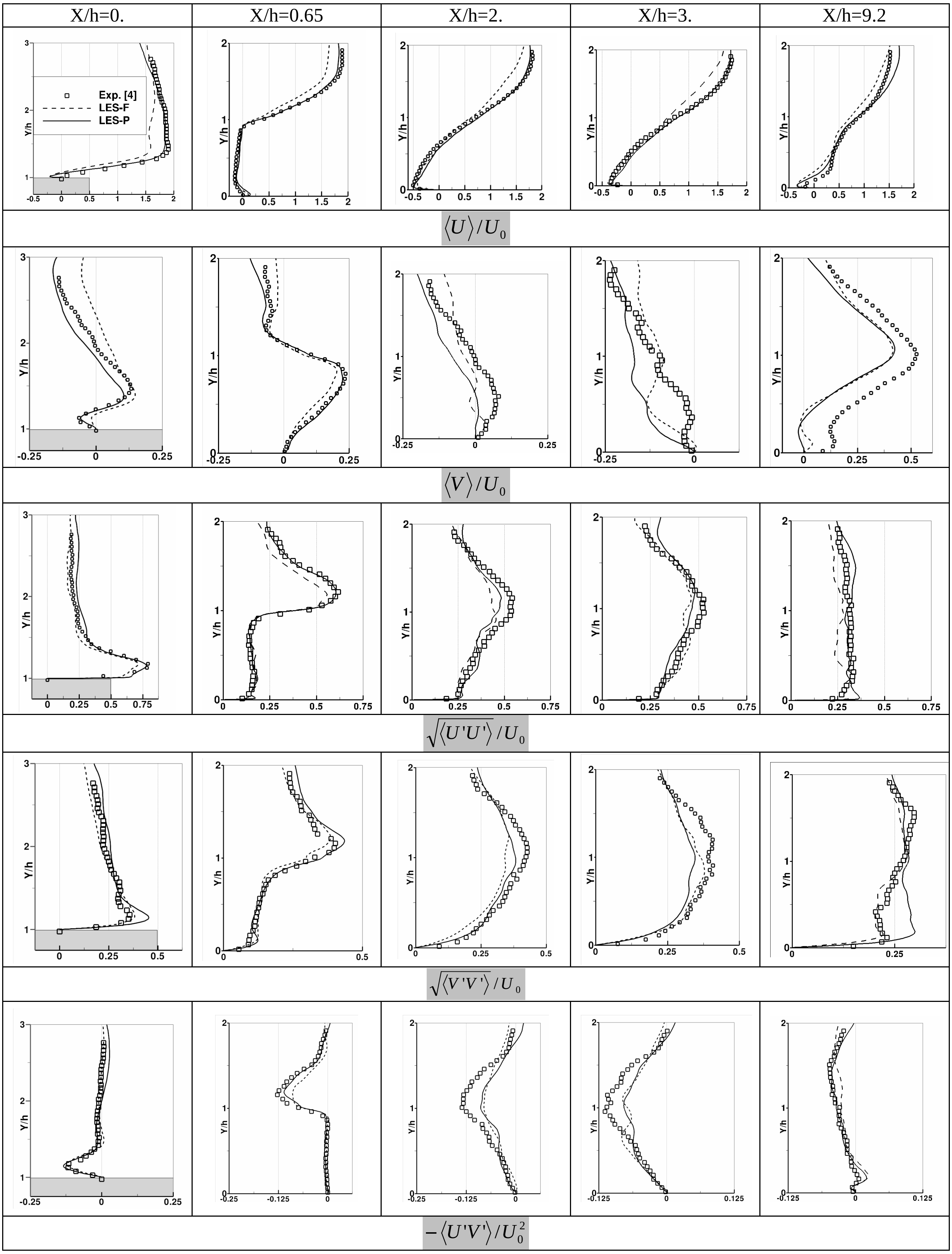

Figure 5: Mean velocity and resolved turbulent quantities profiles at center plane for different sections for both LES compared with experimental data of Casarsa [4].

Fig. 5 shows mean velocity and high-order statistics profiles at the center plane Z/h=0 at the following five axial locations: X/h=0, 0.65, 2, 3 and 9.2 obtained from LES-F and LES-P and compared with experimental data. These axial locations have been chosen in order to cross the different recirculation zones around the rib and on top of the rib and in the the recirculation bubble. The different profiles consist in the normalized mean streamwise U_{mean},<U>/U_0 and cross-stream V_{mean},<V>/ U_0 velocity profiles, resolved U_{rms} $\sqrt{\langle U'U'\rangle}/U_0$, V_{rms} $\sqrt{\langle V'V'\rangle}/U_0$ and resolved turbulent shear stress - <U'V'>/U_0^2. From the plots, it can be seen that the LES-F underpredicts U_{mean} in the channel center. Near the wall, both simulations agree quite well with the experimental data except the location upstream of the rib, where the measurements display a smaller recirculation zone. The cross-stream V_{mean} <V>/ U_0 velocity profiles look spread out, but they are close to 0 and the scale change makes appear variations. In the main recirculation zone, the values are more scattered. The measured U_{rms} profiles show peaks, which arise from shear layer turbulent generation at the rib top surface and decrease, as the flow moves downstream. The LES-P captures the peaks better than the LES-F. However, for the location X/h=9.2 which is upstream of the rib, the resolved U_{rms} profiles are spread out. In the near-wall regions, upstream, above the rib and downstream of the rib, the LES-P over predicts the resolved V_{rms}. For the resolved turbulent shear stress - <U'V'>/U_0^2, the values are very weak and some discrepancies between LES and experimental data are noticeable in the channel center. Globally, the LES-P results seem in better agreement with experimental data than those obtained from LES-F. This could be due to the mass flow rate imposed in the periodicity case, which better represents the experiments. In the case of the full domain, the boundary conditions imposed at the domain entrance is difficult to evaluate because little information is given by the experiments. If we compare the mass flow rates at the same location obtained by both simulations, the one from the full simulation is weaker than the one imposed in the periodic simulation.

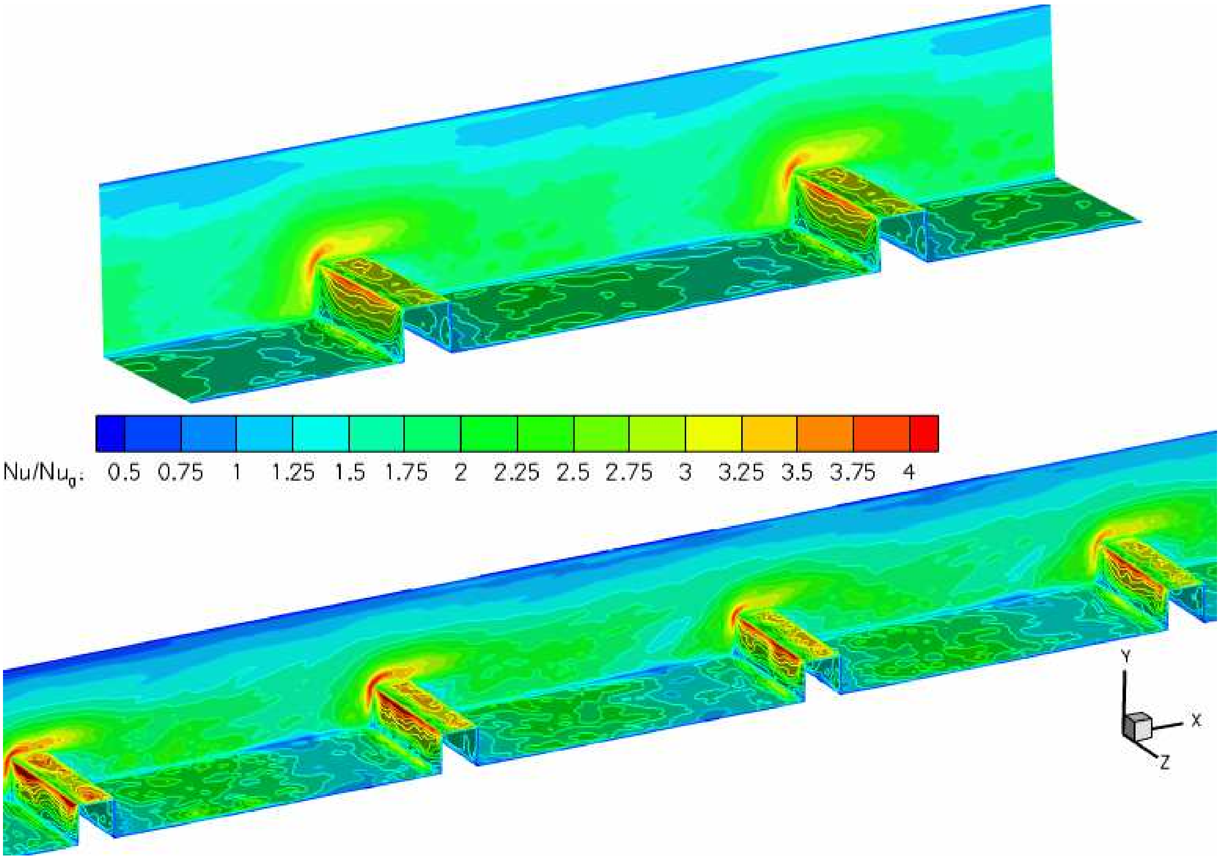

Figure 6: Distribution of Nusselt number on ribbed wall, lateral wall and rib for LES-P (top) and LES-F (bottom).

The heat transfer results (LES-P) are presented in terms of an enhancement factor which corresponds to the ratio between Nusselt number Nu of the flow at the wall $Nu = q_w D_h / \lambda(\theta_w - \theta_{ref})$ and Nu_0 obtained from Dittus-Boelter correlation: $Nu_0 = 0.023\ Re^{0.8}\ Pr^{0.4}$. The results of LES-P (top) and LES-F (bottom) are plotted in Fig. 6 on the different walls of the computational domains and present the same trends between the full and periodic domains. On the bottom wall, the heat transfer is maximum in front of the rib, which is a result of the highly unsteady secondary eddies. These vortices enhance mixing and increase heat transfer coefficient. At the side wall the high values of Nusselt number are located in the vicinity of the rib junction, which is a result of lateral impingement on the wall as shown in Fig. 3. On the rib itself, the heat transfer is high at the top leading edge as a result of the strong fluid acceleration, and in the reattachment region. Immediately downstream from the rib, the heat transfer is low and downstream in the main recirculation region the Nusselt number increases, but does not reach the peaks previously described. The secondary flows play a major role in the heat transfer at the side walls, but there is no experimental data on them. Fig. 7 compares the Nusselt number on the bottom wall (included ribs) for both simulations with the one obtained experimentally [4] around 4th rib. Between the two ribs, both LES underpredict the Nusselt number, whereas on the rib top, the levels are comparable.

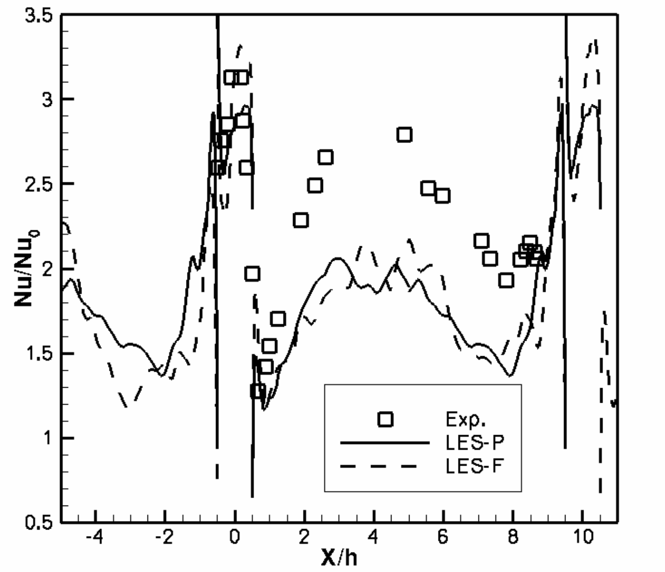

Figure 7: Distribution of Nusselt number on ribbed wall in the center of channel, for the two LES compared with experimental data of Casarsa et al. [4].

Conclusion

Two simulations, a full domain and a periodic domain have been performed in a ribbed square duct with a rib height to hydraulic diameter ratio of .3 and a rib pitch to rib height ratio of 10 for a bulk Reynolds number of 40,000. The present study validates the use of LES for predicting flow and heat transfer with experiments. The small size of the first cell on the bottom (y_1^+) and lateral (z_1^+) walls leads to DNS-like representation of the flow. The simulation reproduces the major flow structures measured experimentally with a very good agreement, namely a recirculation zone formed on the top of the rib and behind the rib, the lateral impingement of the flow on the side walls. After the flow reattachment, the boundary layer grows up and impinges on the rib forming another vortex.

The three-dimensional nature of the flow is very evident. The blockage induced by the rib forces the flow in front of the rib to swirl in the sidewall tube transporting it over the rib in an upward motion. This motion is compensated in the central part of the duct by a downward current, fueled by a streamwise elongated couple of counter-rotating structure in the upper part of the duct. It is observed that the rib induces a flow swirling towards the sidewalls before passing away on top of the rib. As stated above, the contour plots of mean velocities at the center plane illustrate the good agreement of the LES results with experiment. The resolved turbulent profiles are very sensitive in the different recirculation zones, which occur in this kind de geometry. The LES performed in the periodic domain seems closer to experimental data than the one, which computes the full domain. These discrepancies could be related to the inlet boundary conditions in the full domain, which does not represent the experiments, while a flow rate close to experiments, is maintained in the periodic configuration. In front of the rib unsteady vortical structures draw fluid in towards the side wall and induce high values of W_{mean} and W_{rms}. The sidewalls have a strong influence on the heat transfer distribution. The streamlines connecting bottom wall of the rib and a region over the top corner of the rib are well correlated to the high values of heat transfer. While the heat transfer on the ribbed wall is enhanced due to the streamwise flow, the secondary flow plays a major role in the heat transfer on the side walls. Immediately behind the rib, a secondary recirculation is trapped between the wall and the primary recirculation zone, which prevents the fluid from efficiently mixing with the fluid in the channel core, but increases the heat transfer on the downstream rib side. In front of the rib on the ribbed wall, the heat transfer is high as the result of highly unsteady secondary eddies produced in this region.

References

[1] Arun, K., and Prabhu, S.V. 2007. Effects of aspect ratio, channel orientation, rib pitch-to-height ratio and number of ribbed walls on pressure drop characteristics in a rotating channel with detached ribs. *Int. J. of Rotating Machinery*, ID 72190.

[2] Boris, J.P., Grinstein, F.F., Oran, E.S., and Kolbe, R.L. 1992. New insights into large eddy simulation. *Fluid dynamics research*, 10, pp. 199-228.

[3] Çakan, M. 2000. Aero-thermal investigation of fixed Rib-roughened internal cooling passages. PhD. Thesis von Karman Institute & Université Catholique de Louvain (Belgique),.

[4] Casarsa, L. Çakan, M. and Arts, T. 2002. Characterization of the velocity and heat transfer fields in an internal cooling channel with high blockage ratio. Proceedings of the ASME Turbo Expo 2002 June 3-6, Amsterdam, The Netherlands.

[5] Chandra, P.R. Alexander, C.R. and Han, J.C. 2003. Heat transfer and friction behaviours in rectangular channels with varying number of ribbed walls. *Int. J. Heat Mass Transfer*, 46, pp. 481-495.

[6] Graham, A., Sewall, E. and Thole, K. A. 2004. Flowfield measurements in a ribbed channel relevant to internal turbine blade cooling. Proceedings of the ASME Turbo Expo, Vienna, Austria, Paper n0 GT2004-53361.

[7] Gupta, A. SriHarsha, V. Prabhu, S.V. and Vedula, R.P. 2008. Local heat transfer distribution in a square channel with 900 continuous, 900 saw tooth profiled and 600 broken ribs. *Experimental Thermal and Fluid Science*, 32, pp. 997-1010.

[8] Han, J.C. 1988. Heat transfer and friction characteristics in rectangular channels with rib turbulators. *ASME J. Heat Transfer*, 110, pp. 321-328.

[9] Larchevêque, L. Sagaut, P. Mary, I. Labbé O. and Comte, P. 2003. Large-eddy simulation of a compressible flow past a deep cavity. *Phys. of Fluids*, Vol. 15, 1, pp. 193-210.

[10] Liou, T.M. Hwang, J. J. and Chen S.T. 1993. Simulation and measurement of enhanced turbulent heat transfer in a channel with periodic ribs on one principal wall. *Int. J. Heat and Mass Transfer*, 36(2), pp. 507, 517.

[11] Liu, H. and Wang J., 2011. Numerical investigation on synthetical performances of fluid flow and heat transfer of semiattached rib-channels. *Int. J. Heat Mass Transfer*, 54, pp. 575-583.

[12] Lohász, M.M., Rambaud, P. & Benocci, C., Flow features in a fully developed ribbed duct flow as a result of LES, Proceedings of the ERCOFTAC International Symposium on Engineering Turbulence Modelling and Measurements ETMM6 Sardinia, Italy, 23-25 May, 2005.

[13] Murata, A. and Mochizuki, S. 2000. Large eddy simulation with a dynamic subgrid-scale model of turbulent heat transfer in an orthogonally rotating rectangular duct with transverse rib turbulators, *Int. J. Heat and Mass Transfer*, 43, pp. 1243-1259.

[14] Sewall, E.A., Tafti, D.K., Graham A.B. and Thole, K.A. 2006. Experimental validation of large eddy simulations of flow and heat transfer in a stationary ribbed duct. *Int. J. of Heat and Fluid Flow*, 27, pp. 243-258.

[15] Tafti, D.K., 2005. Evaluating the role of subgrid stress modelling in a ribbed duct for the internal cooling of turbine blades, *Int. J. Heat and Fluid Flow*, 26, pp. 92-104.

[16] Tanda, G. 2004. Heat transfer in rectangular channel with transverse and V-shaped broken ribs. *Int. J. of Heat and Mass Transfer*, 47, pp. 229-243.

[17] Viswanathan, A.K. and Tafti, D.K. 2006. Detached eddy simulation of flow and heat transfer in fully developed rotating internal cooling channel with normal ribs. *Int. J. of Heat and Fluid Flow*, 27, pp. 351-370.

[18] Watanabe, K. and Takahashi, T., 2002. LES simulation and experimental measurement of fully developed ribbed channel flow and heat transfer, Proceedings of the ASME Turbo Expo June 3-6, Amsterdam, The Netherlands.

[19] Won, S. Y. and Ligrani, P. M. 2004. Comparisons of flow structure and local Nusselt numbers in channels with parallel- and crossed-rib turbulators. *Int. J. of Heat and Mass Transfer*, 47, pp. 1573-1586.